CORA Cork Open Research Archive
Cartlann Taighde Oscailte Chorcaí

Title	A general method for controlled nanopatterning of oxide dots: a microphase separated block copolymer platform
Authors	Ghoshal, Tandra;Shaw, Matthew T.;Bolger, Ciara T.;Holmes, Justin D.;Morris, Michael A.
Publication date	2012-05-01
Original Citation	Goshal, T.; Shaw, M. T.; Bolger, C. T.; Holmes, J. D.; Morris, M. A. (2012) 'A general method for controlled nanopatterning of oxide dots: a microphase separated block copolymer platform'. Journal of Materials Chemistry, 22 :12083-12089.
Type of publication	Article (peer-reviewed)
Link to publisher's version	https://pubs.rsc.org/en/content/articlelanding/2012/jm/c2jm30468f - 10.1039/C2JM30468F
Rights	© The Royal Society of Chemistry 2012
Download date	2026-11-08 02:45:35
Item downloaded from	https://hdl.handle.net/10468/6781

UCC
University College Cork, Ireland
Coláiste na hOllscoile Corcaigh

A general method for controlled nanopatterning of oxide dots: microphase separated block copolymer platform

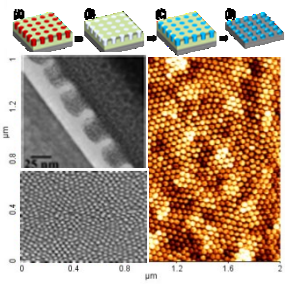
Tandra Ghoshal,[1] Matthew T. Shaw,[2] Ciara T. Bolger,[1] Justin D. Holmes,[1,3] Michael A. Morris[1,3*]

[1]Materials Research Group, Department of Chemistry and Tyndall National Institute, University College Cork, Cork, Ireland

[2]Intel Ireland Ltd., Collinstown Industrial Estate, Co. Kildare, Ireland

[3]Centre for Research on Adaptive Nanostructures and Nanodevices (CRANN), Trinity College Dublin, Dublin, Ireland

Table of contents:



We demonstrate a facile, generic method for the fabrication of highly dense long range hexagonally ordered thermally stable various inorganic oxide nanodots on different substrates by using a microphase separated polystyrene-b-poly(ethylene oxide) (PS-b-PEO) block copolymer thin film as a structural template. The method does not require complex co-ordination chemistry and instead involves the simple, solution based chemistry applicable to a wide range of systems. The feature sizes can be easily tuned by changing the concentration of the precursors.

* To whom correspondence should be addressed: E-mail: m.morris@ucc.ie, Tel: + 353 21 461 948, Fax: ++353 21 474097

A general method for controlled nanopatterning of oxide dots: microphase separated block copolymer platform

Tandra Ghoshal,[1] Matthew T. Shaw,[2] Ciara T. Bolger,[1] Justin D. Holmes,[1,3] Michael A. Morris[1,3*]

[1]Materials Research Group, Department of Chemistry and Tyndall National Institute, University College Cork, Cork, Ireland

[2]Intel Ireland Ltd., Collinstown Industrial Estate, Co. Kildare, Ireland

[3]Centre for Research on Adaptive Nanostructures and Nanodevices (CRANN), Trinity College Dublin, Dublin, Ireland

Corresponding Author Footnote:

Prof. Michael. A. Morris

E-mail: m.morris@ucc.ie

Tel: + 353 21 461 948

Fax: ++353 21 474097

We demonstrate a facile, generic method for the fabrication of highly dense long range hexagonally ordered various inorganic oxide nanodots on different substrates by using a microphase separated polystyrene-b-poly(ethylene oxide) (PS-b-PEO) block copolymer (BCP) thin film as a structural template. The method does not require complex co-ordination chemistry (between metal precursors and the polymer) and instead involves the simple, solution based chemistry applicable to a wide range of systems. A highly ordered PS-b-PEO thin film with perpendicularly oriented PEO cylinders is fabricated by solvent annealing over wafer scale. PEO cylinders are activated by ethanol to create a functional chemical pattern for nanodot development via spin coating and block selective metal ion inclusion. Subsequent UV/ozone treatment forms an ordered arrangement of oxide nanodots and removes the polymer components. The phase purity, crystallinity and thermal stability of these materials coupled to the ease of production may make them useful in technological applications. This method is particularly useful because the feature sizes can be tuned by changing the concentration of the precursors without changing the molecular weight and concentration of the block copolymer.

Introduction

Highly dense, well-ordered arrays of functional nanostructured materials at substrate surfaces is not only scientifically interesting but also technologically important area due to potential applications in optoelectronic devices, information storage, photonic materials, catalysis and sensors.[1-6] Most of these applications require the nanostructures to be chemically stable, uniform in size, well-dispersed and chemically/structurally controlled. Further, the spatial locations of the nanopattern over an extended area should be defined as precisely as possible. The fabrication of nanopatterned materials with ultra-small dimensions has been accomplished by several methods, including self-organisation, ultra-violet or e-electron beam lithography, X-ray lithography or imprint lithography.[7-9] The self-assembly (microphase

separation) of block copolymers is an interesting methodology due to their potential to form highly regular structures of mesoscopic dimensions, bridging the gap between molecular and macroscopic scales.[10-11] Thin films of cylinders (one block hexagonally arranged in a matrix of the other block(s)) forming diblock copolymers have excited particularly interest because; if the cylinders can be oriented perpendicularly to the substrate surface, selective etching procedures can remove the cylinders provide a nanoporous template film.[12-15] A significant challenge for BCP methods is obtaining films with long range order due to the presence of topological defects such as dislocations and disclinations which limit the persistence lengths of the spontaneously formed microdomains.[16]

It has recently been reported that atomic layer deposition of volatile aluminium precursors can be used for selective incorporation of aluminium moieties into a BCP system. Subsequent dry etching can be used to yield an alumina pattern.[17] Selective polymer/metal precursor functionalization has also been used to coordinate metal species.[16] However, these methods are generally relatively complex, involve expensive fabrication equipment and limited in the materials sets that can be used. In this paper we describe a novel, widely applicable and simple methodology to produce oxide nanopatterns based on a simple solvation process rather than complex chemical co-ordination between metal precursors and one of the polymer blocks.[18] It does not require the creation of a nanoporous template[19] or the use of sol-gel methods.[20] The methodology is based on the use of solvent-induced microphase separation in PS-b-PEO thin films which have controlled structure orientation[21] and advantages of the marked difference in the chemical selectivity of PS and PEO to allow selective metal ion inclusion.[22] Different methods (viz. ozonolysis, UV degradation, reactive ion etching and chemical etching) are generally used for selective removal of the minority block in BCPs but the poor degradability of PEO prevents simple generation of nanopores from PS-b-PEO without significant pattern damage.[23-24] This method avoids the need for

selective removal of the PEO block which is challenging. A key advantage of the process is that thermal processing of an oxide precursor is not required during nanodot generation and, thus, not comprising spatial control of the features formed. E.g. sol-gel chemistry a widely used method of generating spatially templated inorganic metal oxide structures[24-25] cannot be used here since oxide formation occurs subsequent to softening, melting, pyrolysis and combustion of the polymer and template confinement is not successfully achieved. In this work, we use a UV/ozone treatment to crosslink and convert non-volatile inorganic compounds into oxides whilst simultaneously removing organic components.

Experimental

A polystyrene-b-poly(ethylene oxide) (PS-b-PEO) diblock copolymer was purchased from Polymer Source and used without further purification (number-average molecular weight, M_n, PS = 42 kg mol^{-1}, M_n, PEO = 11.5 kg mol^{-1}, M_w/M_n = 1.07, M_w: weight-average molecular weight). Substrates used were reclaimed 8" silicon (100) wafers with a native oxide layer. Substrates were cleaned by ultrasonication in acetone and toluene for 30 min each and dried under a nitrogen stream. PS-b-PEO was dissolved in toluene to yield 0.9 wt% polymer solution at room temperature and this solution was aged for 12 hours. The PS-b-PEO thin film was fabricated by spin coating the polymer solution at 3000 rpm for 30 sec on Si wafer. The film was exposed to toluene/water (50:50, v/v) mixed vapour placed at the bottom of a closed vessel kept at 50^{0}C for 1h to induce mobility and allow microphase separation to occur. Separate reservoirs were used for each solvent to avoid azeotropic effects. The resultant phase separated film was immersed in ethanol at 40^{0}C for 15h. For the fabrication of different oxide nanodots, nitrate precursors were used. Here we have used iron (III) nitrate nonahydrate ($Fe(NO_3)_3,9H_2O$), cerium nitrate hexahydrate ($Ce(NO_3)_3,6H_2O$) and copper nitrate hemipenta hydrate ($Cu(NO_3)_2,2.5H_2O$). Different concentrations of precursors were dissolved in ethanol and spin coated onto the nanoporous film. After drying, UV/Ozone

treatment was used in order to oxidize the precursor as well as to remove polymer residues. The oxide nanodots on substrates were placed in a pre-heated oven at different temperature for 1 hour to check the thermal stability of the nanodots.

Surface morphologies were imaged by scanning probe microscopy (SPM, Park systems, XE-100) in tapping mode and scanning electron microscopy (SEM, FEI Company, FEG Quanta 6700). The film thicknesses were measured by optical ellipsometer (Woolam M2000) and electron microscopy. Samples were prepared for TEM cross sectional imaging with an FEI Helios Nanolab 600i system containing a high resolution Elstar™ Schottky field-emission SEM and a Sidewinder FIB column and were further imaged by transmission electron microscopy (TEM, JEOL 2100). X-Ray photoelectron spectroscopy (XPS) experiments were conducted on a Thermo K-alpha machine with an Al K_α x-ray source. All binding energies were referenced to an adventitious C 1s signal at 285.0 eV. FTIR spectra were recorded on infrared spectrometer (Nicolet 6700).

Results and discussion

A diagram of the fabrication process is shown in Scheme 1. A hexagonal arranged microphase separated BCP film (Scheme 1A) was treated with ethanol causing 'activation' of the PEO cylinders (Scheme 1B). The chosen metal ion solution was then spin-coated onto the film and diffuses within the PEO structures driven by capillary solution forces (Scheme 1C). UV/Ozone treatment was carried out to convert the precursor into oxide as well as for complete degradation of the residual polymers (Scheme 1D).

As coated PS-b-PEO films exhibited a mixed orientation of PEO cylinders i.e. parallel and perpendicular orientation with respect to the substrate, with little sign of ordering. Previous works suggests that the polar PEO layer will preferentially wet the substrate surface (favourable PEO-substrate interactions) whilst PS will segregate to the air interface to form a PS-rich layer (PS has a lower surface energy, γ_{PS} = 33 mNm^{-1}; γ_{PEO} = 43 mNm^{-1}). Solvent

annealing[25] in a mixed toluene/water environment was used to induce long range-ordering and favour vertical cylinder orientation. Here, since the room temperature vapour pressure of toluene (P_{vp} = 0.0342 bar) and water (P_{vp} = 0.0313 bar) are similar, swelling and increased mobility in both blocks is achieved and the similarity of the PS-toluene and H_2O-PEO solvent parameters should negate the strong segregation of PS to the surface[26]. Fig. 1a shows an AFM image of the film (40 nm thick as determined by ellipsometry) demonstrating the vertically orientated hexagonal arrangement expected. The minor component, PEO, forms the cylindrical domains (darker contrast in AFM) and the major component, PS, constitutes the matrix (lighter contrast in AFM). The measured average centre-to-centre cylinder spacing is 42 nm with a PEO cylinder diameter is 19.3 nm. The strong multiple peaks in the FFT pattern shown in the inset of Fig. 1a confirms microphase separated structure with highly ordered hexagonal arrangement of PEO cylinders. The SEM image in Fig. 1b also depicts long range ordering of the PS-PEO thin film. Note that various substrates (mica, glass, quartz and SiO_2) were employed to investigate the influence of polymer/substrate interface on structure formation. No significant difference was observed on the substrates, suggesting that the pairwise surface tensions of the films on all substrate are similar.

When the solvent annealed films were ethanol treated at 40^0C for 15 h, modification of the film occurred although the structural arrangement and dimensions are unchanged. Note that longer exposure to ethanol and higher temperatures resulted in structural degradation. The AFM image (Fig. 1c) shows some increase in the phase contrast and an increase in long-rage order. This is also indicated by the Fourier transform of the AFM image (inset Fig. 1c) where six-point patterns with multiple higher order reflections are shown, characteristic of exceptional long-range order. Also, the SEM image contrast was enhanced by ethanol exposure as seen in Fig. 1d. No thickness loss was observed after the ethanol treatment as measured by optical ellipsometry. The ethanol treatment is a pre-requisite to form well-

defined oxide nanopatterns in later steps and is described as an 'activation step'. It is unlikely that very significant solution of PS or PEO occurs (mineral acids such as HI are required for ether cleavage[24]) but some enhancement of PEO at the surface is occurring as revealed by FTIR and XPS spectra (See Supporting Information). We suggest that after solvent annealing the surface remains PS rich and a wetting layer exists. On exposure to ethanol, there is a slow change in structure that removes this thin wetting layer through film re-structuring. It is suggested that this ethanol activation process also displaces water (from the solvent annealing process) from the PEO cylinders. Significant amounts of water are expected to be present as PEO is an important hydrogel forming polymer.[27] It is clear that ethanol removal of the water is slow because of the PEO-water affinity. Note that the exposure conditions were chosen to optimise the nanodot formation process which became less structurally specific with temperature/time suggesting the film could develop a PEO wetting layer prior/during structural degradation. It was also important to dry the films and carry out cation inclusion as quickly as possible presumably to minimize adventitious water uptake.

FIB-thinned cross-sectional TEM data before and after the ethanol activation process support the conclusions made above and are shown in Figs. 1e and 1f respectively. TEM derived thickness of the solvent annealed PS-PEO film before and after ethanol treatment is unchanged and consistent with ellipsometry measurement. This shows that this treatment does not damage the material to any extent. It is not possible to reveal the arrangement of PS and PEO in the non-ethanol treated film due to lack of contrast difference between them. The density of PS (1.05 g cm^{-3}) and amorphous PEO (1.12 g cm^{-3}) are similar and the density of PEO will be reduced further by water content.[28] It is, therefore, clear that the solvent annealing procedure prevents crystallisation of the PEO and minimizes density related TEM contrast differences in the non-ethanol treated films. Fig. 1f shows the large area view of the cross-sectioned nanoporous film after ethanol treatment. It reveals the ordered structural

arrangement of the film generated by ethanol treatment. The measured diameters and depths of the PEO-derived regions were 20 nm and 28 nm respectively (Inset of Fig. 1f). The apparent contrast difference seen here may arise from a number of factors including some solubility of PEO but this is expected to be very limited as described above. In Fig. 1f a distinct contrast line can be seen at the top of the film suggesting much of the PEO is still present, as suggested by the FTIR and XPS data (See Supporting Information). It is suggested that the contrast derives from crystallization of the PEO which can occur during ethanol dehydration. Crystalline PEO has much greater density (1.24 g cm^{-3})[28] and the presence of crystalline polymers is associated with enhanced polymer contrast.[29] It should be noted that PEO does crystallize at 40^0C.[28] What is also apparent in the film following the ethanol treatment is the formation of a coherent polymer across the whole of the substrate surface. This might be explained by the existence of a PS wetting layer which seems unlikely on the basis of the preferred substrate-PEO interactions unless it is a bi-layer consisting of PS and PEO. The upper layer of PS would protect the underlying PEO layer from ethanol exposure just preventing dehydration and crystallisation. Alternatively, it may simply be that ethanol exposure is ceased prior to complete PEO treatment. We could not explore further because of loss of film integrity as described above.

Oxide nanodots are formed by simple inclusion of metal ions (in a metal nitrate ethanol solution) into the PEO component. The hydrophobic nature of PS excludes any probability of the metal ion inclusion into the PS template, so that the PEO activated sites can be considered as sorbtive cylinders with diameter 20 nm and depth 28 nm. PEO is known to have good affinity with cations[27] and it is believed that swelling of PEO by ethanol allows rapid incorporation of the metal cations or perhaps colloidal entities into these active cylinders. This phenomenon can be compared with the diffusion of metal ions into the nanoreactor specific for the metal ion selected.[30-31] But, the mechanism of cation (viz. Cu^{2+})

inclusion is probably via either intra- or intermolecular coordination via electron donation from the PEO block oxygen atoms as shown below.



The tendency towards multiple binding would be favoured by densely packed PEO chains and might explain why the crystalline phase is necessary for effective inclusion of the metal species. No metallic phase viz. Cu(0) was observed just after spin coating the metal precursor solution. The effectiveness of this simple solution mediated inclusion is again good evidence for the presence of PEO. Had complete removal of the PEO been achieved, it would be highly unlikely that significant metal uptake would occur because the PS matrix would be hydrophobic and the concentration of metal in solution is rather low.

After metal ion inclusion, UV/ozone treatment was carried out immediately so as to remove any solvent, oxidize and cross-link metal ions forming oxide and remove the organic part simultaneously. Alternatively, UV/Ozone to cross-link the metal ions followed by air calcinations can also be pursued for oxidation and complete removal of the residual polymer. Note that direct annealing can cause disorders and agglomerations between the nanodots. Unlike nanoreactor synthesis, the matrix or template can be removed to form pure phase of oxides.[30] Fig. 2 shows the AFM and SEM images of well-ordered oxide nanodots of various metal oxides formed after the UV/ozone treatment. From the AFM and SEM images, the measured average centre-to-centre nanodot distance is 42 nm and the FFT pattern shown in the inset of Fig. 2a confirms the hexagonal ordering of the nanodots. This confirms these have been produced via direct templating of the PS-b-PEO film. Fig. 2a (AFM) and 2b (SEM tilt image) shows iron oxide nanoparticles (0.4 wt% iron nitrate ethanol solution) of average diameter 24 nm. The height measured by ellipsometry is 9 nm (in good agreement with TEM

data, see below). The density of the nanodots on the substrate was approximately 4.2 x 10^{10} nanodots cm^{-2}.

In order to examine the route is applicable to prepare well-ordered nanodots of different oxides; the same process was repeated with several inorganic precursors. AFM and SEM images (Figs. 2c and 2d) shows cerium oxide nanodots with a similar long range order as the iron oxide materials and with average diameter 25 nm (1 wt% ethanol cerium nitrate solution). Also, data following spin-coating of a 0.5 wt% ethanol-copper nitrate solution is also shown and this generates the same size features of copper oxide (Figs. 2e and 2f). Note that changes in the metal ion solution concentration are needed to give nanodots of similar sizes suggesting rate of cation uptake is species sensitive. These data, and other materials (TiO_2, HfO_2, CoO, NiO etc.) made in the laboratories show that this is a facile and generic means to generate size monodisperse, hexagonally arranged nanodots at a substrate surface.

The nanodots formed using these methods are well-adhered to the substrate and thermally robust. Typical data is presented in the inset of Fig. 2b which shows iron oxide nanodots after air calcination at 800^0C for 1 h, revealed the ordered structure of the nanodots. The only effect of heating was a reduction in the average diameter and height consistent with high temperature densification and from all the materials studied. In the case of iron oxide nanodots on Si substrates, the diameters and heights were found to reduce by 3 nm and 2 nm respectively for the air calcination at 800^0C for 1 h presumably due to some sintering and, hence, densification. The arrays of copper oxide and cerium oxide nanodots on Si substrate were examined to be thermally stable at temperatures 800^0C and 1000^0C respectively. It can be concluded that the thermal stability of the nanodots depends on the material properties of the nanodot material and the nature of the substrates.

The structure of these systems is exemplified further by TEM (Fig. 3). The cross-sectional TEM image shows well-separated nanodots (Fig. 3a). The adhesion of the materials is

reflected in integrity of the structures during FIB treatment and the lack of any interfacial cracks etc. at the base of the particles. The same cylindrical-type structure is seen for all imaged nanodots. The average diameter and height of the nanodots are 24 nm and 9 nm using a 0.4 wt% nitrate solution. These are consistent with measurements made above. The high resolution TEM (HRTEM) image of one of the nanodots (Fig. 3b) shows the nanodot-substrate interface. The nanodots are supported on a 1.7 nm thick amorphous native at the silicon substrate surface. Although the lattice fringes are not very clear from the HRTEM image, but revealing its single crystalline nature. To further study the crystalline nature, the nanodots on Si substrate were scratched by a sharp edge blade and disperse into ethanol for the preparation of TEM grid. Clear lattice fringes can be seen from Fig. 3c revealed the single crystalline nature. The lattice fringes were regularly separated with a spacing of 0.2967 nm, which agrees well with the (220) lattice index of cubic Fe_3O_4 (inset of Fig. 3c).[32]

The diameter and height of the nanodots can be varied by changing the polymer molecular weight and composition. However, the simplest approach is to vary the concentration of precursor solution which changes the size of the nanodots without changing their spacing or structural arrangement. This is illustrated in Figs. 4a, b and c, where well-ordered copper oxide nanodot arrays can be seen after UV/Ozone treatment. The average diameters 18, 24 and 30 nm generated from 0.3, 0.5 and 0.7 wt% ethanol-copper nitrate solutions. It can also be estimated from the SEM images that the height of the nanodots is increasing with higher precursor concentration. It should be noted that at metal ion solution concentrations exceeding 1% for the copper system result in the deposition of localised agglomerated 3D nanoparticle structures across the substrate surface. This is ascribed due to over-filling of the PEO cylinders. Generally spin coating involves convection of a coating liquid, driven by centrifugal force and evaporation of the solvent simultaneously.[33] After spin coating at room temperature, there is always some residual solvent remaining on the film surface because of

surface tension effects and also due to slower evaporation rate of ethanol (some amount of water present). When the precursor solution concentration is low, the metal ions diffused and interact with the PEO cylinders implying the absence of any metals ions with the residual precursors left on the surface just after spin coating. But, with increasing the precursor concentrations to a certain extent, the amount of unreacted metal ions increases and present with the residual precursors on few areas of the film surface in the form of a droplet which oxidized upon exposure to the UV/Ozone. The surface density of these 3D structures was observed to increase with increasing solution concentration (Fig. 4d). An excessive metal precursor concentration might results oxide depositions all over the substrate. Similar limiting solution concentrations were seen for all the oxides investigated. This overloading of material is consistent with the proposed preferential PEO solution inclusion model since if this was a simple template mechanism, it would be expected that these non-specific surface depositions would be seen throughout the solution concentration range.[34]

To verify the crystalline structure and phases of oxides nanodots, X-ray diffraction (XRD) was attempted but could not differentiate between different phases of that oxide due to poor signal-to-noise ratio (small volume of material present). Alternatively, the materials were further studied by XPS to assess the surface composition and chemical structures of the nanodots following 800^0C calcinations. Fig. 5a shows typical XPS survey spectrum of iron oxide nanodots and confirms the presence of Si, O, C and Fe. The C1s feature is relatively small and demonstrates effective removal of carbon species during processing. Its intensity is consistent with adventitious material formed by adsorption and other contamination during sample preparation. High resolution Fe 2p core level spectrum (inset of Fig. 5a) consists of two sharp peaks associated with Fe $2p_{3/2}$ at 711.3 eV and Fe $2p_{1/2}$ at 725.1 eV accompanied by satellite structures (8 eV shift) on their high binding energy side. These data are consistent with the existence of Fe^{+3} ions only.[35-36] Although the stoichiometry could not be precisely

determined from XPS, it reveals the formation of a majority phase of Fe(III) oxide. Survey spectrum obtained from cerium oxide and copper oxide nanodots on Si substrates also indicates pure oxides without any trace of polymers (data not shown). The XPS Ce 3d spectrum is illustrated in Fig. 5b for the cerium oxide nanodots after annealing. There are six peaks assigned in the spectrum which are complicated by a process known as shake-down and the features are labelled according to the convention established by Burroughs.[37] The peaks U, U″, U‴ and V, V″, V‴ refer to $3d_{3/2}$ and $3d_{5/2}$ respectively and are characteristic of Ce(IV) 3d final states. The high binding energy doublet V‴/U‴ at 916.6 eV and 898.4 eV are assigned to the final state of Ce(IV) $3d^9 4f^0$ O $2p^6$. Doublets V″/U″ at 907.3 eV and 888.6 eV were attributed to the hybridization state of Ce(IV) $3d^9 4f^1$ O $2p^5$, and doublets V/U at 901.0 eV and 882.5 eV correspond to the state of Ce(IV) $3d^9 4f^2$ O $2p^4$. These data indicate that sintering in air results in a Ce(IV) oxide, consistent with a CeO_2 fluorite oriented structure. The XPS spectrum of copper oxide nanodots on Si substrate, Cu 2p core level region is shown in Fig. 5c. The Cu $2p_{3/2}$ and Cu $2p_{1/2}$ peaks centred at 933.7 and 953.6 eV (splitting of 19.9 eV) respectively can be attributed to the presence of the Cu^{2+} chemical state as an indication for formation of CuO.[38] Moreover, the shake-up satellite peaks of the Cu $2p_{3/2}$ and Cu $2p_{1/2}$ at 942.4 and 962.6 eV respectively (~ 9 eV shift) confirmed formation of Cu^{2+} on the surface. [39] Note that the Cu 2p features for CuO and $Cu(OH)_2$ appear almost at the same binding energy but the possibility of forming the hydroxide phase has not been considered because of the high temperature calcination immediately prior to analysis.

4. Conclusions

A simple, generic and cost-effective route was demonstrated to fabricate well-ordered arrays of inorganic oxide nanodots over wafer scale. It can be applied to a number of oxide and substrate materials. The nanodots formed have uniform sizes, shape and are structurally arranged in a mimic of the original self-assembled BCP pattern. It is suggested that the dots

are formed by selective inclusion of a metal ion solution in the hydrophilic PEO cylinders of the microphase separated structure. The nanodots inclusion does not compromise the BCP structure. The size of the oxide nanodots can be controlled by variation of the metal ion solution concentration. The nanodots have good thermal stability and show strong adherence to the surface to high temperatures. The phase purity and compositions of the oxides was confirmed by XPS analysis. We suggest that the structure, crystallinity and thermal stability of these materials coupled to the ease of production may make them useful in many applications. This process could be extended to a wide range of size and spacing of features by use of similar BCPs of varying composition and block sizes.

Acknowledgements

The authors would like to thank Science Foundation Ireland for support of this project through the Strategic Research Cluster FORME grant and the CSET CRANN grant. The contribution of the Foundation's Principal Investigator support is also acknowledged. We are also grateful to a number of technical supports. Dr. N Petkov (Tyndall) and R Dunne (Intel) Irl. for TEM support and Dr. P G Fleming for XPS assistance.

References

[1] H. G. Craighead, *J. Appl. Phys.,* 1984, **55**, 4430-4435.

[2] H. Temkin, G. J. Dolan, M. B. Panish and S. N. G. Chu, *Appl. Phys. Lett.,* 1987, **50**, 413-415.

[3] A. Wiedensohler, H. C. Hansson, I. Maximov and L. Samuelson, *Appl. Phys. Lett.,* 1992, **61**, 837-839.

[4] A. P. Alivisatos, *Science,* 1996, **271**, 933-937.

[5] H. J. Fan, P. Werner and M. Zacharias, *Small,* 2006, **2**, 700-717.

[6] Y. Cui, M. T. Bjork, J. A. Liddle, C. Sonnichsen, B. Boussert and A. P. Alivisatos, *Nano Lett.,* 2004, **4**, 1093-1098.

[7] S. Park, B. Kim, J. Y. Wang and T. P. Russell, *Adv. Mater.,* 2008, **20**, 681-+.

[8] G. M. Wallraff and W. D. Hinsberg, *Chem. Rev.,* 1999, **99**, 1801-1821.

[9] F. Rousseaux, D. Decanini, F. Carcenac, E. Cambril, M. F. Ravet, C. Chappert, N. Bardou, B. Bartenlian and P. Veillet, *J. Vac. Sci. Technol. B,* 1995, **13**, 2787-2791.

[10] Y. N. Xia, J. A. Rogers, K. E. Paul and G. M. Whitesides, *Chem. Rev.,* 1999, **99**, 1823-1848.

[11] J. Bang, U. Jeong, D. Y. Ryu, T. P. Russell and C. J. Hawker, *Adv. Mater.,* 2009, **21**, 4769-4792.

[12] M. Park, C. Harrison, P. M. Chaikin, R. A. Register and D. H. Adamson, *Science,* 1997, **276**, 1401-1404.

[13] C. Park, J. Yoon and E. L. Thomas, *Polymer,* 2003, **44**, 6725-6760.

[14] C. Y. Wang, Y. D. Mao, D. Y. Wang, Q. S. Qu, G. J. Yang and X. Y. Hu, *J. Mater. Chem.,* 2008, **18**, 683-690.

[15] T. Thurn-Albrecht, R. Steiner, J. DeRouchey, C. M. Stafford, E. Huang, M. Bal, M. Tuominen, C. J. Hawker and T. Russell, *Adv. Mater.,* 2000, **12**, 787-791.

[16] E. Huang, P. Mansky, T. P. Russell, C. Harrison, P. M. Chaikin, R. A. Register, C. J. Hawker and J. Mays, *Macromolecules,* 2000, **33**, 80-88.

[17] Y. C. Tseng, Q. Peng, L. E. Ocola, J. W. Elam and S. B. Darling, *J. Phys. Chem. C,* 2011, **115**, 17725-17729.

[18] S. H. Yun, B. H. Sohn, J. C. Jung, W. C. Zin, J. K. Lee and O. Song, *Langmuir,* 2005, **21**, 6548-6552.

[19] Q. Peng, Y. C. Tseng, S. B. Darling and J. W. Elam, *Adv. Mater.,* 2010, **22**, 5129-+.

[20] J. Peng, X. Li, D. H. Kim and W. Knoll, *Macromol. Rapid Commun.,* 2007, **28**, 2055-2061.

[21] P. Mokarian-Tabari, T. W. Collins, J. D. Holmes and M. A. Morris, *ACS Nano,* 2011, **5**, 4617-4623.

[22] D. Kannaiyan, E. Kim, N. Won, K. W. Kim, Y. H. Jang, M. A. Cha, D. Y. Ryu, S. Kim and D. H. Kim, *J. Mater. Chem.,* 2010, **20**, 677-682.

[23] M. F. Zhang, L. Yang, S. Yurt, M. J. Misner, J. T. Chen, E. B. Coughlin, D. Venkataraman and T. P. Russell, *Adv. Mater.,* 2007, **19**, 1571-1576.

[24] H. M. Mao and M. A. Hillmyer, *Macromolecules,* 2005, **38**, 4038-4039.

[25] J. Peng, D. H. Kim, W. Knoll, Y. Xuan, B. Y. Li and Y. C. Han, *J. Chem. Phys.,* 2006, **125**.

[26] J. Peng, Y. C. Han, W. Knoll and D. H. Kim, *Macromol. Rapid Commun.,* 2007, **28**, 1422-1428.

[27] C. B. Tsvetanov, R. Stamenova, D. Dotcheva, M. Doytcheva, N. Belcheva and J. Smid, *Macromol. Symp.,* 1998, **128**, 165-182.

[28] W. Y. Chen, J. X. Zheng, S. Z. D. Cheng, C. Y. Li, P. Huang, L. Zhu, H. M. Xiong, Q. Ge, Y. Guo, R. P. Quirk, B. Lotz, L. F. Deng, C. Wu and E. L. Thomas, *Phys. Rev. Lett.,* 2004, **93**.

[29] G. H. Michler, *Electron Microscopy of Polymers* Springer, 2008.

[30] N. E. Kotel'nikova, E. L. Lysenko, R. Serimaa, K. Pirkkalainen, U. Vainio, A. L. Shakhmin, N. N. Saprykina, V. K. Lavrent'ev, D. A. Medvedeva and N. P. Novoselov, *Russ. J. Appl. Chem.,* 2006, **79**, 1902-1906.

[31] N. Galvez, B. Fernandez, E. Valero, P. Sanchez, R. Cuesta and J. M. Dominguez-Vera, *C. R. Chim.,* 2008, **11**, 1207-1212.

[32] C. Hui, C. M. Shen, T. Z. Yang, L. H. Bao, J. F. Tian, H. Ding, C. Li and H. J. Gao, *J. Phys. Chem. C,* 2008, **112**, 11336-11339.

[33] S. S. Kucherenko and K. D. Leaver, *J. Micromech. Microeng.,* 2000, **10**, 299-308.

[34] R. A. Farrell, N. Petkov, M. A. Morris and J. D. Holmes, *J. Colloid Interface Sci.,* 2010, **349**, 449-472.

[35] P. Mills and J. L. Sullivan, *J. Phys. D-Appl. Phys.,* 1983, **16**, 723-732.

[36] T. Fujii, F. M. F. de Groot, G. A. Sawatzky, F. C. Voogt, T. Hibma and K. Okada, *Physical Review B,* 1999, **59**, 3195-3202.

[37] A. Kotani, T. Jo and J. C. Parlebas, *Adv. Phys.,* 1988, **37**, 37-85.

[38] M. F. Al-Kuhaili, *Vacuum,* 2008, **82**, 623-629.

[39] C. C. Chusuei, M. A. Brookshier and D. W. Goodman, *Langmuir,* 1999, **15**, 2806-2808.

Figure captions:

Scheme 1 Schematic illustration of the fabrication of oxide nanodots. (A) Highly ordered PS-b-PEO thin film prepared by solvent annealed process. (B) Nanoporous template produced by activation of PEO cylinders. (C) metal oxide precursor moves into the cylinders after spin coating the precursor solution. (D) oxide dots remain after UV/Ozone treatment.

Fig. 1 (a, c) Atomic force microscoy (AFM), (b, d) scanning electron microscopy (SEM) and (e, f) cross sectional TEM images of PS-b-PEO thin film solvent annealed in toluene/water at 50^0C and nanoporous template after ethanol treatment respectively. Insets of a and c shows the corresponding FFT pattern. Inset of f shows magnified image of ethanol treated film.

Fig. 2 AFM and SEM images of hexagonal ordered different oxide nanodots after UV/Ozone treatment. (a) and (b) iron oxide; (c) and (d) cerium oxide; and (e) and (f) copper oxide nanodots. Insets of (a) shows the corresponding FFT pattern. Inset of (b) shows iron oxide nanodots annealed at 800^0C for 1h.

Fig. 3 (a) TEM cross-sectional image of iron oxide nanodots. Inset shows the higher magnification image. (b) cross-sectional HRTEM image of a single nanodot. (c) HRTEM image from the nanodots after UV/Ozone treatment. Inset shows crystalline fringes corresponds to Fe_3O_4.

Fig. 4 SEM images of different sized copper oxide nanodots for different concentrations of precursors (a) 0.3%, (b) 0.5% (c) 0.7% and (d) 1.2%.

Fig. 5 (a) XPS survey spectra recorded from the iron oxide nanodots on Si substrate after annealing at 800^0C for 1h. Inset shows high resolution spectrum for Fe 2p core level revealed Fe_2O_3 phase. (b) Ce 3d spectra depict CeO_2 phase and (c) Cu 2p core level spectra describes CuO phase.

Scheme 1

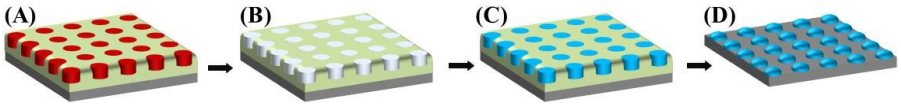


Fig. 1

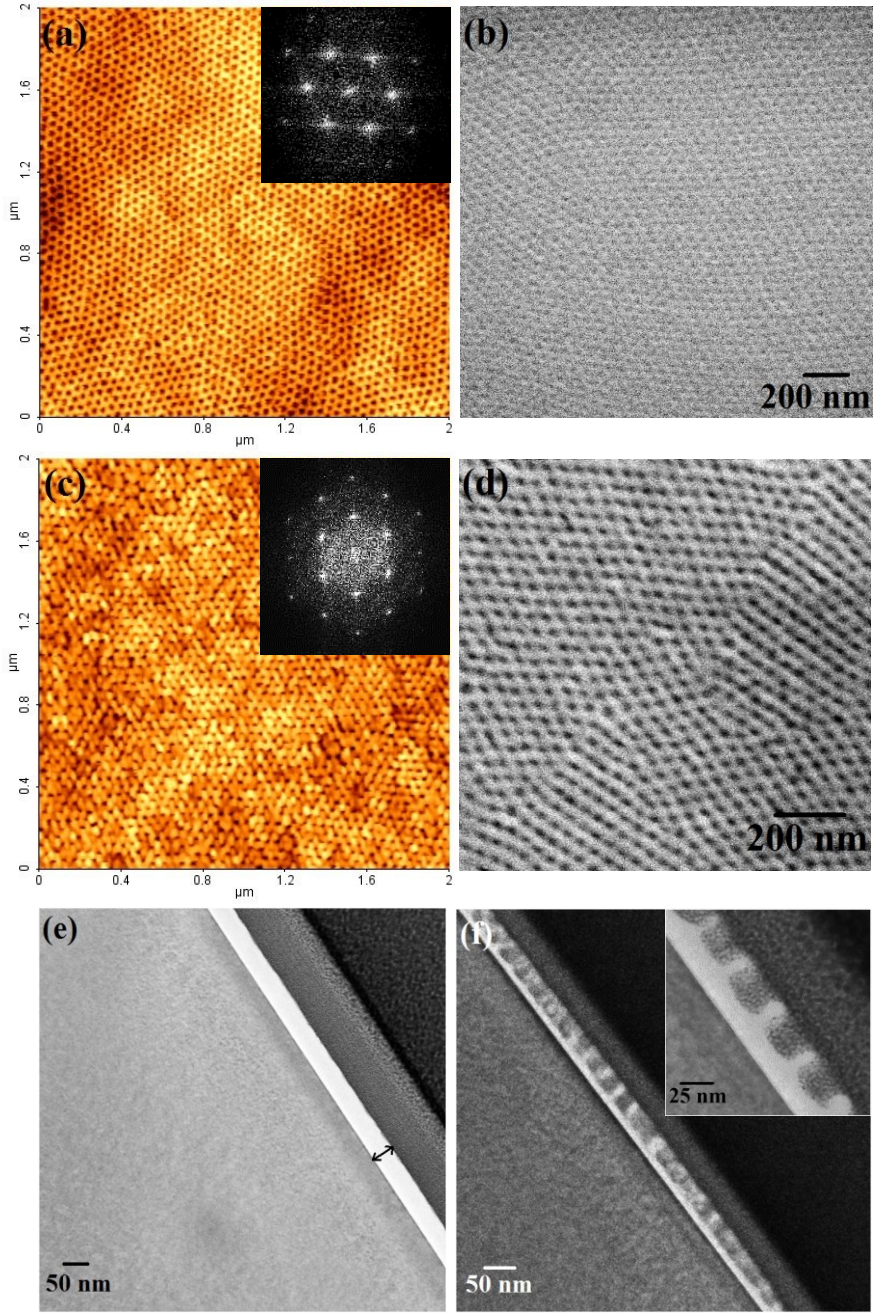


Fig. 2

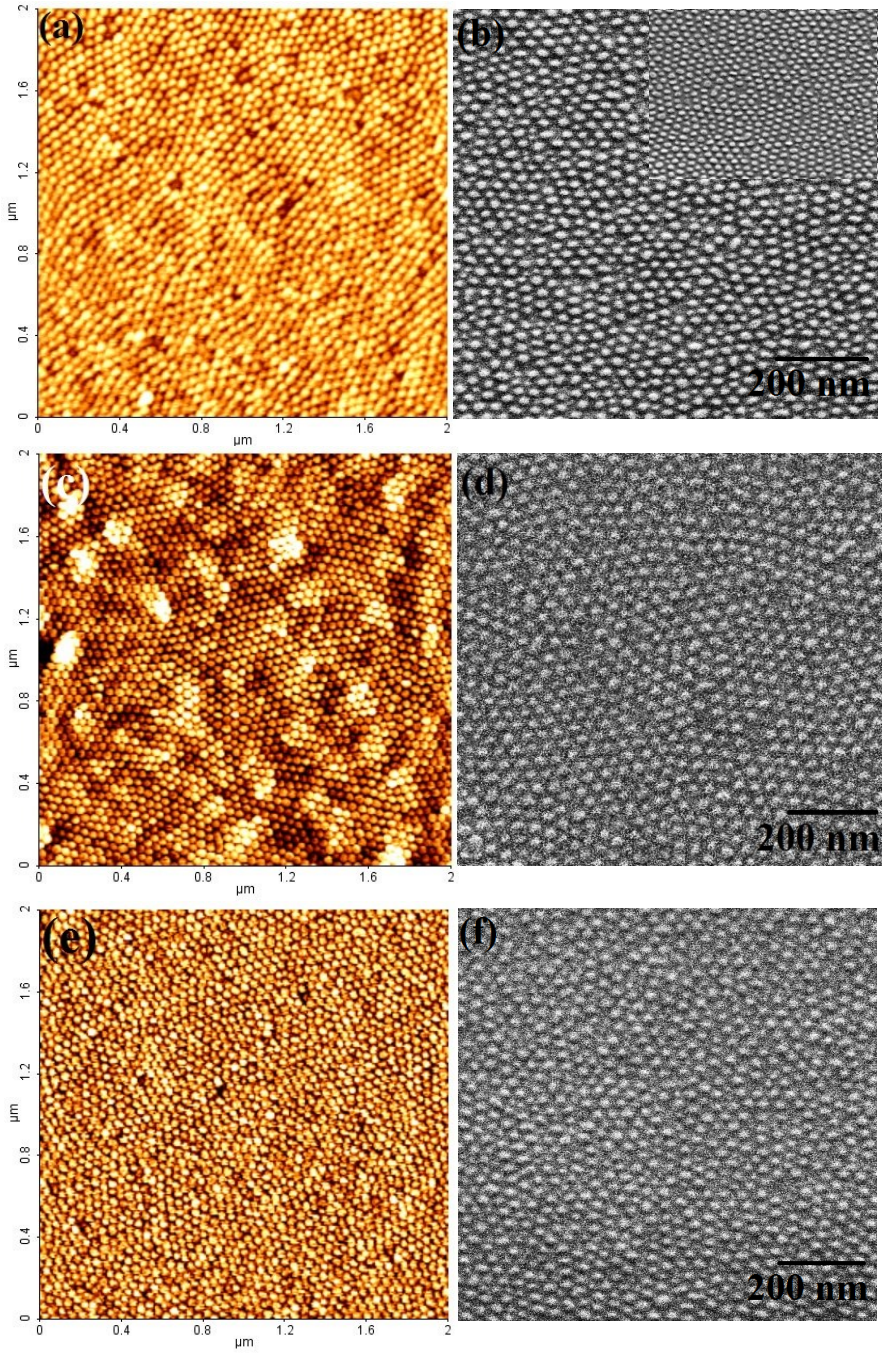


Fig. 3

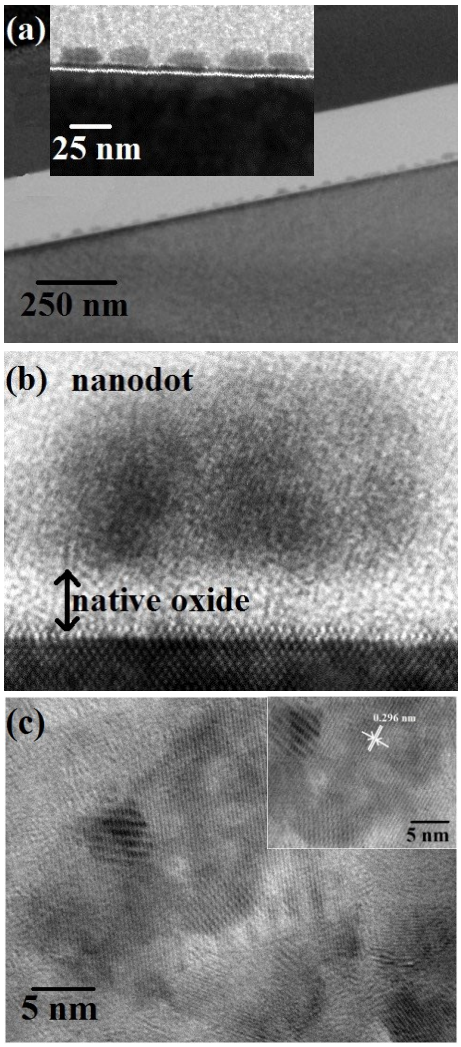


Fig. 4

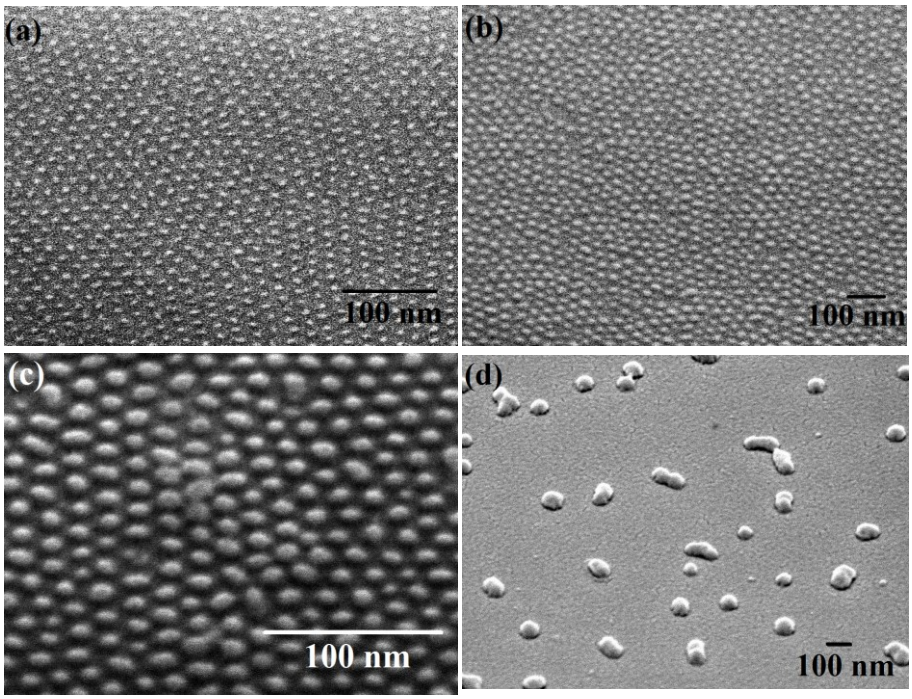
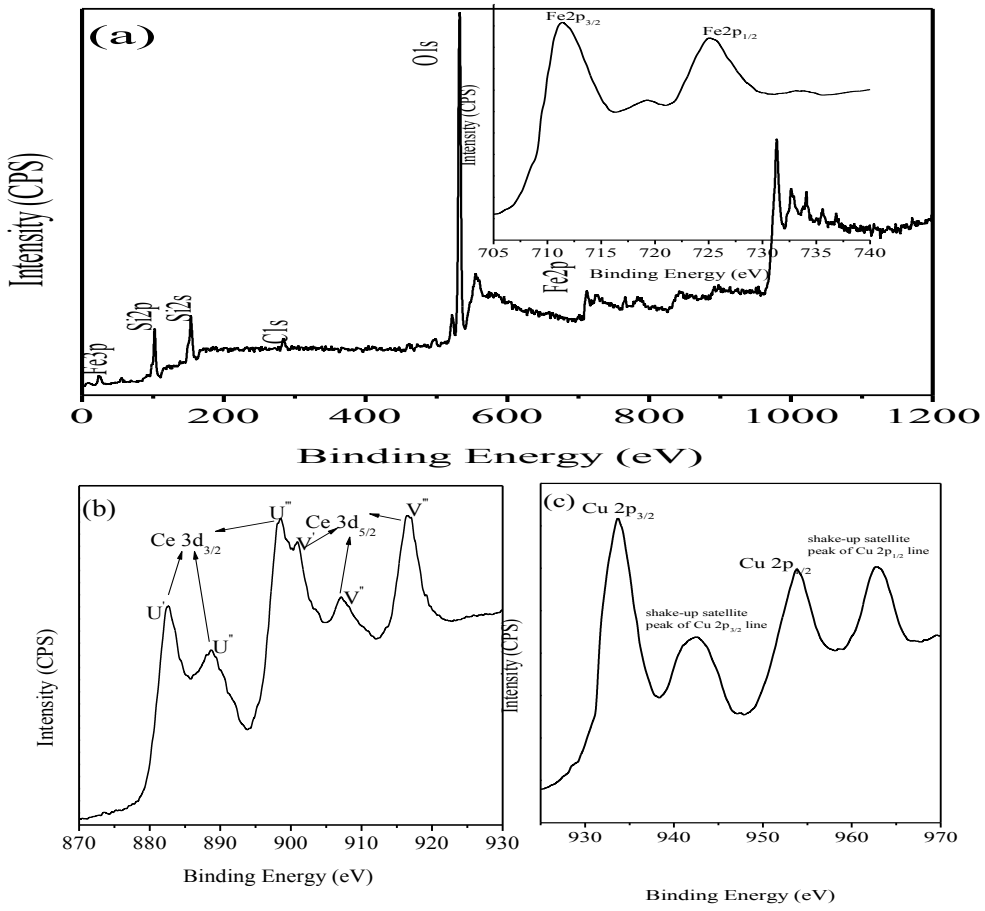


Fig. 5


(a)
Intensity (CPS)
Fe3p
Si2p
Si2s
C1s
O1s
Fe2p
Fe2p3/2
Fe2p1/2
Binding Energy (eV)
0
200
400
600
800
1000
1200
705
710
715
720
725
730
735
740
(b)
Ce 3d3/2
Ce 3d5/2
U'
U''
U'''
V'
V''
V'''
870
880
890
900
910
920
930
(c)
Cu 2p3/2
Cu 2p1/2
shake-up satellite peak of Cu 2p3/2 line
shake-up satellite peak of Cu 2p1/2 line
930
940
950
960
970

Supporting information:

Surface analysis by FTIR. FTIR spectra shown in Fig. S1 provides additional information of the film surface at different experimental conditions. The non-ethanol treated film shows distinct features typical of the PS and PEO blocks (Fig. S1(a)). Peaks at between 763 cm^{-1} (benzene bending) and 1602 cm^{-1}, 1494 cm^{-1} and 1452 cm^{-1} (benzene ring stretching), weak overtone and combination bands in the range of 1655-2000 cm^{-1} as well as features at 3000-3100 cm^{-1} (C-H stretching in benzene) can all be attributed to polystyrene.[1] The features at 1102 cm^{-1} (C-O-C stretch), 924 cm^{-1} (CH_2 PEO rocking modes), and 1749 cm^{-1} and 1720 cm^{-1} (C=O stretches of the ester and keto group respectively) as well as peaks at 2925 cm^{-1} and 2854 cm^{-1} (CH_2 PEO stretching modes) can all be assigned to the PEO block.[2] It is apparent that on ethanol activation, the PS derived features decrease in relative intensity compared to those of PEO (Fig. S1(b)). FTIR data of copper oxide nanodots after UV/Ozone treatment and further annealing are shown in Figs. S1(c) and S1(d) which confirms the removal of polymer content. Two features can be seen at 1084 and 1010 cm^{-1} which can be assigned to transverse optical phonon mode in -Si-O-Si-[3] and the Si-O-Cu phonon mode[4].

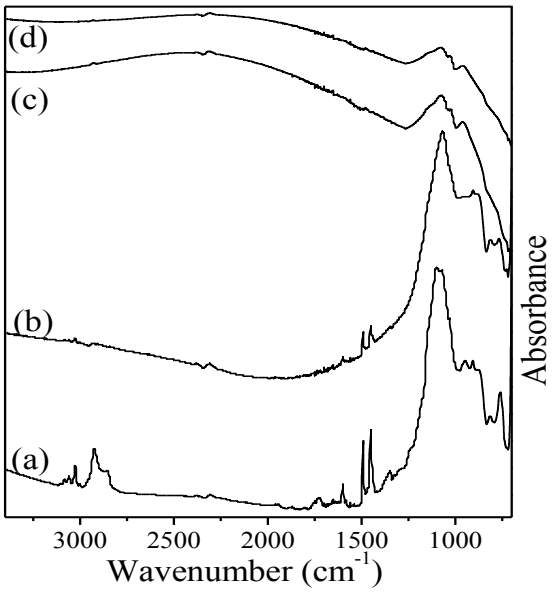


Fig. S1. FTIR spectra of (a) PS-PEO hexagonal dot patterns after solvent annealing, (b) nanoporous PS template after ethanol treatment (c) copper oxide nanodots after UV/Ozone treatment and (d) copper oxide nanodots after UV/ozone along with annealing.

(1) K. Ibrahim, A. Salminen, S. Holappa, K. Kataja, H. Lampinen, B. Lofgren, J. Laine and J. Seppala, *J. Appl. Polym. Sci.* 2006, **102**, 4304-4313.

(2) F. Ahmad, M. K. Baloch, M. Jamil and Y. J. Jeon, *J. Appl. Polym. Sci.* 2010, **118**, 1704-1712.

(3) C. T. Kirk, *Physical Review B* 1988, **38**, 1255-1273.

(4) C. Thambidurai, Y. G. Kim, N. Jayaraju, V. Venkatasamy and J. L. Stickney, *J. Electrochem. Soc.* 2009, **156**, D261-D268.

Surface analysis by XPS. In order to further explore the surface composition, XPS analyses were performed for PS-PEO film before and after ethanol treatment. The C1s peak of PS-PEO before and after ethanol treatment can be curve-fitted to reveal four components as illustrated in Figs. S2a and S2b. They are attributed to carbon from the aromatic ring of PS (**C**-(C,H)$_{arom}$) at 284.9 eV, carbon from the aliphatic backbone of PS (**C**-(C,H)$_{aliph}$) at 285.2 eV, carbon involved in an ether link (**C**-O-**C**) from PEO at about 286.5 eV and, finally, a shake-up satellite peak associated with the aromatic ring of PS (**C**$_{sh\ up}$) at about 291.5 eV. Since the C-O-C component only comes from the PEO block and the rest of the carbon components are solely attributed to the PS block, it can be concluded that the PEO block is less present at the outermost surface for the PS-PEO film in comparison with its proportion for the ethanol treated film. Quantification of peak areas suggests that the relative concentration of PEO block increases from 14% to 19% during the ethanol treatment of PS-PEO film. The corresponding survey spectra shown in the inset of Figs. S2a and b also illustrate an increase in the oxygen peak intensity for the ethanol treated film. This again confirms much of the PEO is still present in the film and its surface contribution is enhanced

(as suggested by the FTIR and TEM data). No silicon was detected by the survey spectra that mean the thickness of the film is sufficient to mask the substrate.

Fig. S2. (a, b) C1s core level spectrum of PS-PEO before and after ethanol treatment respectively. In sets of (a, b) shows the corresponding survey spectra.

